

KAIRA: The Kilpisjärvi Atmospheric Imaging Receiver Array—System Overview and First Results

Derek McKay-Bukowski, Juha Vierinen, Ilkka I. Virtanen, Richard Fallows, Markku Postila, Thomas Ulich, Olaf Wucknitz, Michiel Brentjens, Nico Ebbendorf, Carl-Fredrik Enell, Marchel Gerbers, Teun Grit, Peter Gruppen, Antti Kero, Toivo Iinatti, Markku Lehtinen, Henri Meulman, Menno Norden, Mikko Orispää, Tero Raita, Jan Pieter de Reijer, Lassi Roininen, Arno Schoenmakers, Klaas Stuurwold, and Esa Turunen

Abstract—The Kilpisjärvi Atmospheric Imaging Receiver Array (KAIRA) is a dual array of omnidirectional VHF radio antennas located near Kilpisjärvi, Finland. It is operated by the Sodankylä Geophysical Observatory. It makes extensive use of the proven LOFAR antenna and digital signal-processing hardware, and can act as a stand-alone passive receiver, as a receiver for the European Incoherent Scatter (EISCAT) very high frequency (VHF) incoherent scatter radar in Tromsø, or for use in conjunction with other Fenno-Scandinavian VHF experiments. In addition to being a powerful observing instrument in its own right, KAIRA will act as a pathfinder for technologies to be used in the planned EISCAT_3-D phased-array incoherent scatter radar system and participate in very long baseline interferometry experiments. This paper gives an overview of KAIRA, its principal hardware and software components, and its main science objectives. We demonstrate the applicability of the radio astronomy technology to our geoscience application. Furthermore, we present a selec-

tion of results from the commissioning phase of this new radio observatory.

Index Terms—Antenna arrays, phased arrays, radar antennas, radio astronomy, receiving antennas.

I. INTRODUCTION

THE European Incoherent Scatter (EISCAT) radar facility in northern Fenno-Scandinavia [1] is planned to undergo a major upgrade. Termed “EISCAT_3D,” this upgrade project is nearing the end of its preparatory phase and will use modern phased-array technology in place of the radio dishes, which have been used successfully with the current EISCAT system for more than 30 years [2].

The Kilpisjärvi Atmospheric Imaging Receiver Array (KAIRA) was conceived as a technology pathfinder for the EISCAT_3-D project, with the main purpose of demonstrating the capabilities of using modern wide-band phased-array radio telescope technology for incoherent scatter radar measurements. Situated in Arctic Finland, it is designed to be used as a bistatic phased array radar receiver for the current EISCAT VHF incoherent scatter radar transmitter near Tromsø in Norway. A further aim of the KAIRA project was to demonstrate that the technology can be multiuse, i.e., that the same radio receiver could also be used for a large number of other active and passive geophysical remote sensing experiments, which are typically not possible with traditional incoherent scatter radars due to their inherent narrow band nature. It was also anticipated that the application of this technology might enable measurements hitherto impossible with existing systems.

The antenna and signal processing system chosen for KAIRA is the same as that used in the Low-Frequency Array (LOFAR) International Telescope, a radio telescope network intended for low-frequency astronomy, designed and produced by the Netherlands Institute for Radio Astronomy (ASTRON) and Dutch industry [3]. This choice was motivated by the fact that the development work on LOFAR had already been completed, that the system was already tested, that a large international user community existed for support and that it gave an opportunity to evaluate a general-purpose radio astronomy design for use with atmospheric/ionospheric applications. The LOFAR system is a

Manuscript received August 6, 2013; revised January 14, 2014 and May 26, 2014; accepted July 21, 2014. The KAIRA facility was funded by the Infrastructure Funds of the University of Oulu. The development work to be carried out at the KAIRA platform was supported by the European Regional Development Funds of Lapland through the Regional Council of Lapland, and by the 7th Framework Preparatory Phase project “EISCAT_3D: A European Three-Dimensional Imaging Radar for Atmospheric and Geospace Research.” The work of I. I. Virtanen was supported by the Academy of Finland (application number 250252 “Measurement Techniques for Multi-Static Incoherent Scatter Radars”). The work of C.-F. Enell was supported by the EU 7th Framework Infrastructures project 283676, Near-Earth Space Data Infrastructure for e-Science (ESPAS). This work has been funded by the Academy of Finland (application number 250215, “Finnish Programme for Centres of Excellence in Research 2012–2017”).

D. McKay-Bukowski is with the Sodankylä Geophysical Observatory, University of Oulu, 99600 Sodankylä, Finland and also with Rutherford Appleton Laboratory, Harwell-Didcot, Oxfordshire OX11 0QX, U.K. (e-mail: derek.mckay-bukowski@sgo.fi).

J. Vierinen is with Sodankylä Geophysical Observatory, University of Oulu, 99600 Sodankylä, Finland and also with the MIT Haystack Observatory, Westford, MA 01886 USA (e-mail: x@mit.edu).

I. I. Virtanen is with the Department of Physics, University of Oulu, 90014 Oulu, Finland (e-mail: ilkka.i.virtanen@oulu.fi).

R. Fallows, M. Brentjens, N. Ebbendorf, M. Gerbers, T. Grit, P. Gruppen, H. Meulman, M. Norden, J. P. de Reijer, A. Schoenmakers, and K. Stuurwold are with the ASTRON, 7990 AA Dwingeloo, The Netherlands (e-mail: fallows@astron.nl).

M. Postila, T. Ulich, C.-F. Enell, A. Kero, T. Iinatti, M. Lehtinen, M. Orispää, T. Raita, L. Roininen, and E. Turunen are with the Sodankylä Geophysical Observatory, University of Oulu, 99600 Sodankylä, Finland.

O. Wucknitz is with Max-Planck Institut für Radioastronomie, D-53121 Bonn, Germany.

Digital Object Identifier 10.1109/TGRS.2014.2342252

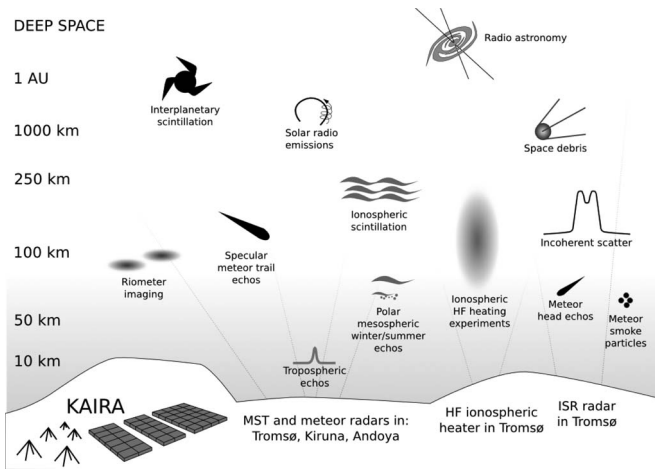


Fig. 1. Figurative overview of the science objectives of KAIRA.

phased array with no moving parts, which is beneficial in an Arctic environment. Additionally, LOFAR has been designed for mass-production of low-cost components that are moderately quick to deploy and commission. The system permits rapid pointing with multiple beam formation and has high sensitivity. Furthermore, the broad-band nature of this system also ensures that many different transmitters can be received with the hardware.

What KAIRA sets out to achieve is the application of radio astronomy technology to geoscience applications such as riometry, incoherent scatter radar and ionospheric scintillation measurements. The location of KAIRA provides a superior site for radio observations of these, and other, solar-terrestrial processes. In our exposition of the science goals and demonstration of our first results, we set out the geophysical applications of this system and science areas that can be tackled, which are not covered in the standard literature on LOFAR, or other similar radio-telescope concepts.

This paper provides a technical description of the facility, its capabilities and the first scientific results that have been accomplished.

II. SCIENTIFIC AIMS

The scientific aims of KAIRA are illustrated in Fig. 1 and are broadly categorized into active and passive measurements. The primary aim for the project is to accomplish multibeam bistatic incoherent scatter radar measurements, and we show the results of this in this paper.

Active measurements are made in conjunction with transmissions from other facilities, either coordinated or as by-products of other transmission motivations, including ionospheric modification measurements that are made in conjunction with the EISCAT Tromsø HF heating facility [4]–[6]. Multistatic micrometeor head echo trajectory measurements [7] will be possible in conjunction with the Tromsø VHF radar, and specular trail echoes in association with any of the many Mesosphere–Stratosphere–Troposphere and meteor radars. It is also planned to image high signal-to-noise-ratio radar targets, such as Naturally Enhanced Ion-Acoustic Line events and to track artificial hard radar targets (large debris and satellites).

Passive measurements include interplanetary scintillation [8], [9], solar radio emission studies, e.g., [10], ionospheric scintillation [11], multistatic, multifrequency measurements of polar mesospheric winter and summer echoes [12], and wide-band imaging riometry. Although the primary use is not radio astronomy, astronomical measurements are still planned, as KAIRA can be used to increase significantly the longest baseline of the LOFAR Very Long Baseline Interferometry (VLBI) network [13]. The facility complements other planned or existing radio telescopes (such as SKA [14], [15], MWA [16], [17], LWA [18], LOFAR [3]), providing demonstration test beds, validation and cross-checking and accomplishing cross-discipline astrophysical/geophysical science goals.

III. DESCRIPTION

The KAIRA station comprises two arrays of 48 dual-polarization antennas; the low-band antenna (LBA) array covers a nominal frequency range of 10–80 MHz and the high-band antenna (HBA) array covers a nominal 110–270 MHz. The intervening gap is the broadcast allocation of FM radio, which is deliberately excluded. Recent advances in digital signal processing and computing are utilized, resulting in the rapid control of these antennas using digital multibeamforming techniques.

A. Site Selection and Preparation

The general location was chosen as a site within Finnish territory, with good transport access, and at a distance from the EISCAT radar transmitter at Ramfjordmoen, near Tromsø, so as to permit a suitable observing angle for bistatic incoherent scatter measurements ($\approx 45^\circ$ at 80- to 100-km altitude above the transmitter). The region is remote and has relatively little radio-frequency interference (RFI) compared with the rest of Europe.

The facility requires a stable ground surface. For this the site of roadworks spoil was chosen, providing a relatively flat, stable surface, which was easy to work on, not subject to tundra ground shift and yet without huge slabs of rock. The elevation of this mound above the surrounding tundra also provided a wind-shear effect over the site, which assists in the natural clearing of snow.

The site was roughly leveled, then an initial layer of coarse gravel was placed. The depth of this was approximately one meter, with some variation due to the underlying terrain. In this, plastic drain pipes were embedded to minimize the amount of water (and thus ice shift) that would occur. This layer was then leveled again and a fine gravel packing soil was placed over the top of this adding a further depth of 10 cm.

B. Construction

The site was identified in the summer of 2010, with testing occurring during the first winter there and construction took place during the summers of 2011 and 2012. The station was completed in August 2012, as shown in Fig. 2 and became operational in September 2012. The planned operational life-time of the project is at least one complete solar cycle (11–12 years).



Fig. 2. Newly completed KAIRA site. Photograph by Arttu Jutila, August 2012.



Fig. 3. HBA tile antennas (#83 and #96) on the timber framesets. The material at the base of the frameset is a strip of geotextile, used to prevent erosion along the array edges and between the tiles.

In addition to the KAIRA instrument, the site has a simple office, storage, mobile network connectivity and power. A perimeter fence is installed to keep reindeer away from the antennas. The site is close to many other scientific facilities as well as local infrastructure, access roads, and communication.

C. Antenna Arrays

The antennas used in the two arrays have been designed to optimize their performance and deployment within their designed frequency range.

The 48 HBAs each comprise 16 1-m-wide crossed-bowtie antenna elements packed into a plastic-covered, polystyrene frame, to form “tiles.” The elements are spaced 1.25 m apart and the azimuthal orientations of the polarizations are $+X = 137^\circ$ and $+Y = 47^\circ$. In the base of each tile is an earthed metal wire grid to serve as a common ground plane. Each tile is 5 m by 5 m and stands approximately 0.5 m tall. In the case of LOFAR stations, these are placed directly on level ground and are anchored to the ground with rotating metal locks at the end of nylon lines. For KAIRA, it was not desirable to have the tiles placed as such due to drifting snow and the difficulties presented in terms of cable installation and protection. Instead, as shown in Fig. 3, the tiles were mounted on “framesets”, i.e., open timber lattices, which stand 1.5 m tall. Each tile is placed on top of a frameset and connects directly to it with elastic. The framesets are then anchored to the ground in the same



Fig. 4. LBA array with aerial #35 in the foreground. The black “cap” at the top of the post contains two low-noise amplifiers (one per polarization).

manner as conventional LOFAR systems. The ability to connect the anchors to arbitrary points on the timber frameset makes it even easier to effect the deployment of these systems over uneven soil. The use of the framesets raises the top of the tiles 2 m above the mound-level (which itself is raised some 5–7 m above the surrounding landscape). This increased elevation allows a natural clearing of light snow due to the wind shear.

The signals from the 16 crossed-bowtie antenna elements within each HBA tile are combined with a remotely controlled analog beamformer. Thus, each of the 48 tiles still only has two outputs, one for each polarization. Because of the size and number of receiving sub-elements, these are packed within each tile in a regular grid, and the tiles themselves are also regularly spaced across the field.

The 48 LBAs are crossed inverted-V-dipole aeriels, standing 1.8 m tall, above a 3 m by 3 m steel grid ground plane, as shown in Fig. 4. The azimuthal orientations of the polarizations are $+X = 45^\circ$ and $+Y = 315^\circ$. The antennas are scattered in a quasi-random pattern across a field 34 m in diameter to give a good beam-profile with low sidelobes. It matches the layout of the inner section of a LOFAR remote station [3], although without the outlying calibration antennas, enabling direct comparison. Instead, these two additional aeriels are placed within the compact array area at locations selected to improve sidelobe suppression.

Fig. 5 shows the layout of the two antenna arrays. The HBA array layout was chosen as a compromise between beam-pattern for imaging the region of the atmosphere illuminated by the EISCAT radar and ease of construction. The elongation in the direction of the Tromsø transmitter reduces the vertical beam width when pointing that way, with the long-axis baseline corresponding to the maximum achievable in the space without requiring significant extra back-filling of the ground plane. Additionally, the layout is consistent with a 96-antenna layout of a LOFAR international station. This permits KAIRA to be converted to the LOFAR international station layout without requiring the repositioning of existing antennas. Two “snow corridors” between the sections of the array allow for snow accumulation.

The array parameters and coordinates for the centers of the two arrays are presented in Table I.

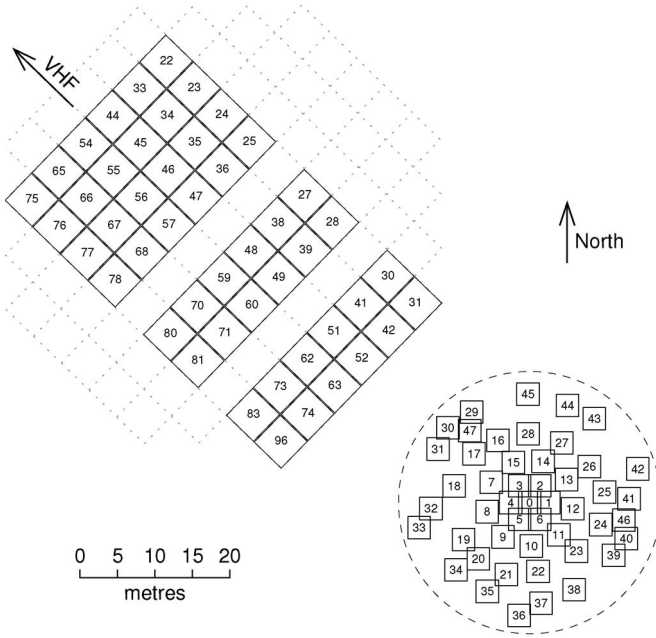


Fig. 5. Scale layout of the KAIRA antennas (with their identification numbers). The HBA array is in the northwest and the LBA array is in the circular area to the southeast. The squares on the LBA array mark the physical extent of the ground-planes. Directions to geographical north and the VHF transmitter at Ramfjordmoen are shown. The dotted lines on the HBA array show the superimposed locations of LOFAR international station tiles [3].

TABLE I
PARAMETERS FOR THE TWO KAIRA ANTENNA ARRAYS. COORDINATES ARE FOR THE ARRAY CENTERS AND ARE GIVEN USING ITRF2005 (epoch = 2013.5) EUREF-FIN. THE GEOGRAPHIC HEIGHT REFERENCE SYSTEM FOR BOTH GRS AND GK/N60 ARE GIVEN

| Parameter | LBA Array | HBA Array |
|---------------------------|----------------------|-----------------------------|
| Number of antennas | 48 | 48 |
| Antenna type | Inverted-V dipoles | 16-element tiles |
| Number of elements | 48 | 768 |
| Polarizations per antenna | 2 linear | 2 linear |
| Array layout | sparse, quasi-random | segmented, rectangular grid |
| Array physical size | 34 m diameter | 30 x 50 m |
| Array alignment | symmetrical | 313.95 degrees |
| Minimum frequency | 8 MHz | 110 MHz |
| Maximum frequency | 80 MHz | 270 MHz |
| RCU modes (c.f. §III-D) | RCU-3 & 4 | RCU-5, 6 & 7 |
| Tile beam-forming | n/a | analog |
| Array beam-forming | digital | digital |
| Longitude | 20.76207580° E | 20.76103311° E |
| Latitude | 69.07074450° N | 69.07105610° N |
| Height (GRS) | 523.371 m | 525.336 m |
| Height (GK/N60) | 493.123 m | 495.086 m |
| Geocentric-X | 2136832.728 m | 2136818.698 m |
| Geocentric-Y | 810088.928 m | 810039.764 m |
| Geocentric-Z | 5935285.442 m | 5935299.217 m |

For both the HBA array and LBA array, two 75- Ω coaxial cables connect each antenna to the electronics cabin. These allow power and control to be sent to each antenna and transport the radio-frequency (RF) signals the other way. The cabin is a regular shipping container that has been fitted with an RF-shielded enclosure to act as a Faraday cage and prevent the enclosed electronics interfering with the arrays.

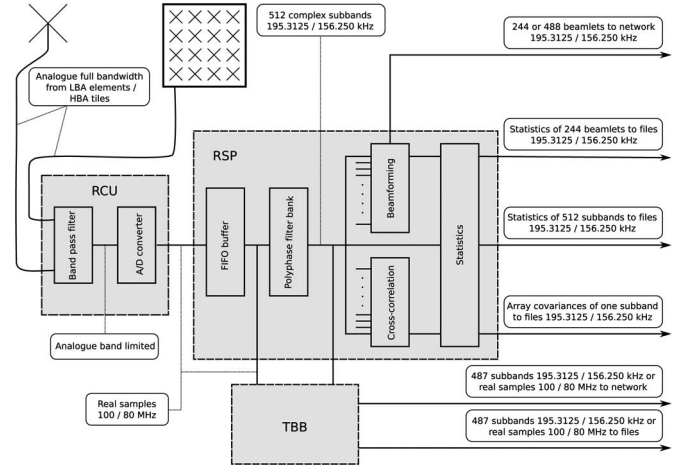


Fig. 6. Functional description of data flow inside the KAIRA station, showing the main RCU, remote signal processing (RSP), and transient buffer board (TBB) components. The unconnected inputs to the beamforming and cross-correlation stages represent equivalent inputs from other antenna/signal-processing chains. Adapted from [20].

D. Signal and Data Processing

KAIRA uses the standard LOFAR signal processing system described in [19] and depicted in Fig. 6. In the RF enclosure, 96 receiver unit (RCU) boards are used to process the incoming signals; one per polarization and per selected LBA or HBA. Each RCU has 3 inputs: one for an HBA signal and two for LBA signals. The LBA inputs are referred to as Low-Band High and Low (LBH and LBL, respectively) for historical reasons, although both have the same frequency capability [3]. KAIRA uses the LBH input with the LBL remaining spare for future expansion. Each RCU provides switches and filters to select the required antenna input and observing frequency band and different combinations of inputs and filters (referred to as RCU modes) can be selected independently for each RCU.

A sampling clock frequency of 200 MHz is typically used, giving Nyquist bands of 100 MHz across. This puts the boundary between the first and second Nyquist zones at 100 MHz, which is within the region occupied by commercial FM-radio station broadcasts (87.5–108.0 MHz), which are a significant source of RFI. The sampler clock can be switched to 160 MHz, which allows access to observing frequencies between 165 and 235 MHz, with the implication that bandwidths are also reduced.

Sampling uses 12-bit analog-to-digital conversion, which gives approximately 3 bits for sky signal and the remainder for electronic offsets, noise and RFI overhead.

The RCU modes are listed in Table II and Fig. 7 shows typical bandpasses. The RFI is clearly visible, particularly the terrestrial short-wave communications below 20 MHz, FM-radio between 87–108 MHz and satellite communications between 240–268 MHz. The most commonly used RCU modes are modes 3, 5, and 7.

After digitization, the signal is split into 512 “subbands” via a polyphase filter bank. Each subband is of equal bandwidth, which is governed by the sampling clock used.

Up to 244 of these subbands, each from an arbitrary set of antennas and for both polarizations, can be selected and

TABLE II

KAIRA RCU MODES. IN MODE 5, THE NOMINAL RECEIVER BAND IS INVERTED (BUT THIS CAN BE CORRECTED LATER IN THE PROCESSING CHAIN). MODE 0 IS USED TO DISABLE AN RCU WITHIN THE CURRENT OBSERVATION. MODES 1 AND 2 ARE CURRENTLY UNUSED, BUT ALLOW FOR FUTURE ALTERNATIVE ANTENNA CONFIGURATIONS

| Mode | RCU input | Nyquist zone | Receiver band (MHz) | Approx. actual passband (MHz) |
|------|-----------|--------------|---------------------|-------------------------------|
| 0 | — | — | — | — |
| 1 | LBL | I | 0–100 | 8–80 |
| 2 | LBL | I | 0–100 | 28–80 |
| 3 | LBH | I | 0–100 | 8–80 |
| 4 | LBH | I | 0–100 | 28–80 |
| 5 | HBA | II | 100–200 | 110–191 |
| 6 | HBA | III | 160–240 | 165–235 |
| 7 | HBA | III | 200–300 | 209–270 |

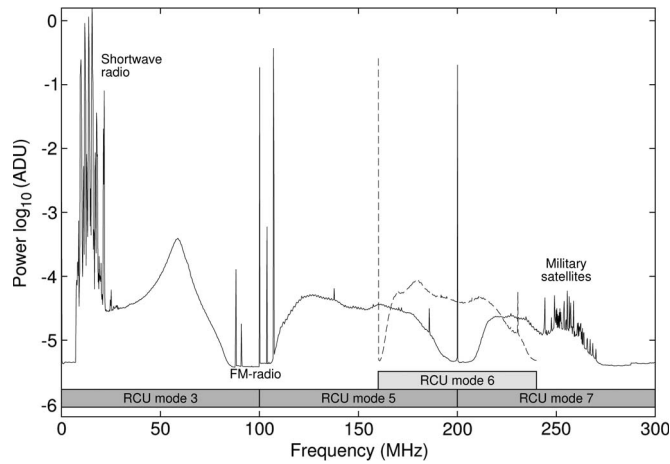


Fig. 7. Combined bandpasses for the common RCU-modes. The dotted line is for RCU-mode 6, which cannot be used simultaneously with the others as it uses a different sampler clock frequency. Prominent sources of interference are marked. The strong lines at exactly 100, 160, and 200 MHz are harmonics of the sampler clock, which appear at the band-edges.

combined into “beamlets” using a complex-weighted, phase-rotated beamformer. Beamlet, i.e., b , is therefore a signal associated with a pointing direction on the sky, (θ, ϕ) , subband, s , from the set of all subbands, S , and an antenna set, A' , from the set of all antennas, A . The set of beamlets, $B \ni b$ can thus be defined as $B = \{(\theta, \phi, s, A') | s \in S \wedge A' \subset A\}$. Choosing which subband for each beamlet is arbitrary. Typically, it is to select a wide separation of frequencies (where measurement at different frequencies yields spectral information), to match third-party transmitter frequencies for incoherent scatter radar experiments, or to avoid particular RFI. The input subband and weighting of each beamlet can be independently set, thus allowing for typical combinations up to 48 MHz in bandwidth ($\Delta\nu$) and up to 244 beamlets [21]. The number of beamlets is determined by the capacity of the field-programmable gate array chips. Reduced-bit sampling, in tradeoff for dynamic range (and thus tolerance to interference), allows 488 or 976 beamlets (for 8- and 4-bit sampling, respectively) and results in increased bandwidth as listed in Table III. The bit reduction is done after separation into subbands. This is important because saturating the reduced dynamic range by RFI will only affect the subbands with RFI. Even strong shortwave radio does not leak into other bands.

TABLE III

SIGNAL-PROCESSING PARAMETERS FOR THE KAIRA FACILITY. THE THREE COLUMNS REFLECT DIFFERENCES WHEN SELECTING DIFFERENT NUMBERS OF SAMPLE BITS. WHERE APPROPRIATE, DIFFERENT VALUES ARE GIVEN FOR THE TWO SAMPLER CLOCK SETTINGS (160 or 200 MHz)

| Parameter | Performance | | |
|----------------------------------|-------------|--------|------------|
| Subbands per RCU | 512 | 512 | 512 |
| Sample bit depth | 12 | 8 | 4 |
| Num. simultaneous beams | 244 | 488 | 976 |
| Polarizations per beam | 2 | 2 | 2 |
| Cumulative $\Delta\nu$ (200 MHz) | 47.7 | 95.3 | 190.6 MHz |
| Cumulative $\Delta\nu$ (160 MHz) | 38.1 | 76.3 | 152.5 MHz |
| Spectral Resolution (200 MHz) | 195.31 | 195.31 | 195.31 kHz |
| Spectral Resolution (160 MHz) | 156.25 | 156.25 | 156.25 kHz |

Because beam-forming takes place after the digitization of the signal, it permits rapid repointing of the array as well as simultaneous observation in multiple directions.

Data products are 1-s power averages of the spectrum from each RCU, 1-s power averages for each beamlet and a correlation matrix, also generated once per second. This correlation matrix contains correlations between all RCU pairs for a single subband. This can be configured to be either a fixed subband, or allowed to cycle through each of the 512 subbands. Additionally, the raw beamlet samples are broadcast as UDP packets at a sampling rate of 200/1024 (or 160/1024) Msample/s for high time resolution observations.

A second local computer is used for accumulation of data products and initial data processing. Initially, KAIRA has only a 2 Mbit/s mobile network link, thus requiring manual recovery of large data sets. However, it is possible to operate the station remotely with no local human presence.

The hardware also includes TBBs, which use random-access memory to store up to 1.3 s of raw data samples, recorded at the full-time resolution (5 ns for a 200-MHz sample clock rate). Data acquisition for the TBB units is continuous with a configurable algorithm used to determine when acquisition should be halted to allow readout. This capability will allow KAIRA to detect fast radio transients or provide high-resolution analysis of received radar signals.

E. System Performance

The beam size of the array is given by $\theta = \alpha\lambda/D$ rad, where λ is the wavelength and the D is the effective array diameter; both in meters. The scaling parameter, α , used is 1.02 ± 0.01 for the HBA array and 1.10 ± 0.02 for the LBA array [3]. The zenith beam sizes are plotted in Fig. 8. The beam size is elongated in the elevation axis by $\sec(Z)$, where Z is the zenith angle.

The reception pattern of the arrays can be approximated by a product of the array pattern, antenna element pattern, and, for the HBA array, a combined tile analog beam. Simulations using code based on established linear inverse problem solving algorithms [22] have been carried out to characterize the response pattern and are shown in Figs. 9 and 10 for typical frequencies for the riometer and incoherent-scatter radar applications. The patterns have been validated using a selection of on-sky drift scans of bright astronomical sources for the LBA array and

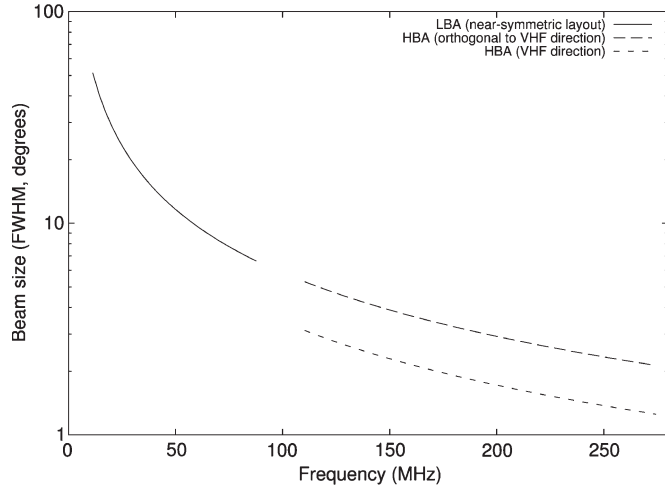


Fig. 8. Zenith beam size for the LBA and HBA arrays. In the case of the HBA, the array dimensions are nonsymmetric leading to a quasi-elliptical beam. All measurements are subject to a $\sec(Z)$ elongation in the vertical axis for nonzero zenith angle, Z .

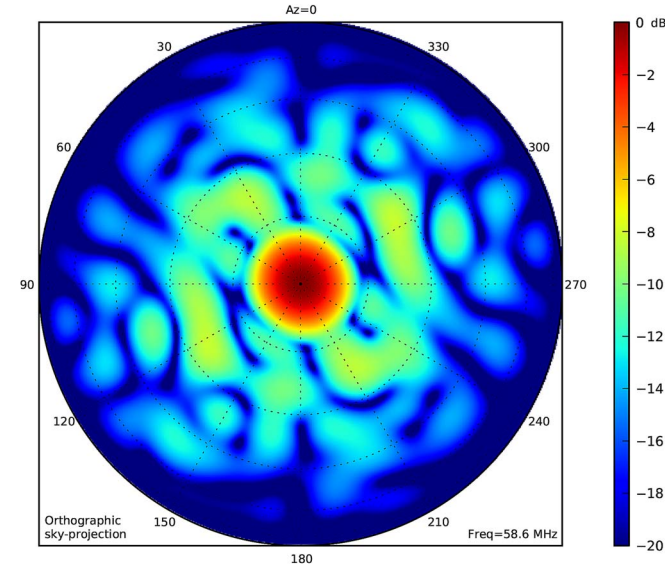


Fig. 9. Simulation of the zenith beam response of the KAIRA LBA array.

both bright sources and 150 MHz beacon transmissions from satellites for the HBA array.

The performance of KAIRA is measured in terms of the system equivalent flux density, defined as $\text{SEFD} = 2kT/A_{\text{eff}}$, where k is Boltzmann's constant, T is the combined system temperature, $T = T_{\text{sky}} + T_{\text{instrument}}$, and A_{eff} is the effective receiving area of the array [23]. As a common system, we apply the same method described in [3], [24] to determine A_{eff} as a function of frequency.

At KAIRA's observing frequencies, the radio sky is dominated by a haze of Galactic synchrotron emission and a couple of bright sources: Cassiopeia A and Cygnus A. Determination of the SEFD for KAIRA uses on-off source measurements against these bright sources, using standard fluxes [25], but correcting for brightness evolution [26]. Off-source positions are chosen to have equivalent beam patterns and lie off the Galactic plane and North Spur, to provide a plain emission

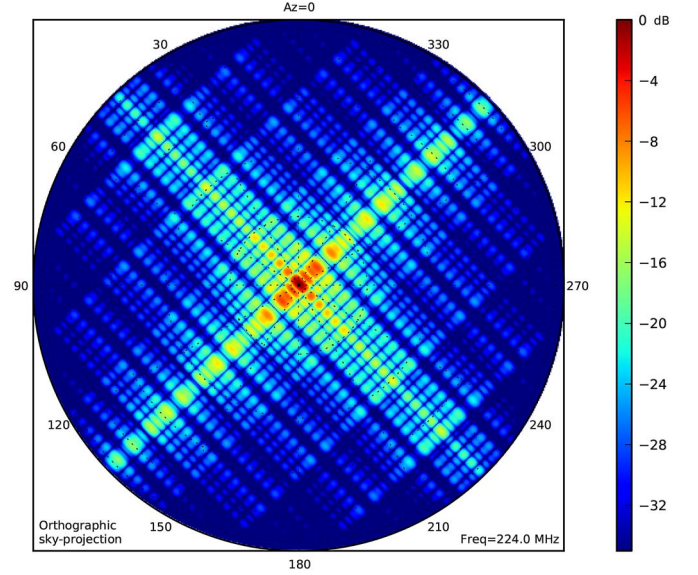


Fig. 10. Simulation of the zenith beam response of the KAIRA HBA array. The regular grid results in a strong grating effect, although this is not problematic for coded, timed incoherent scatter experiments. The effect can be mitigated for radio-astronomy experiments by using tapering.

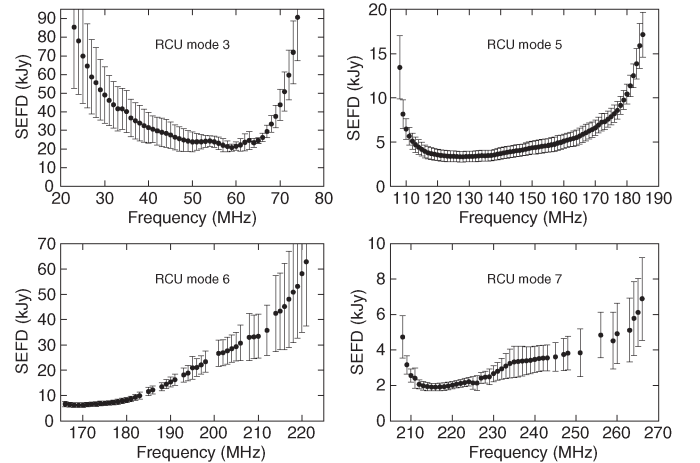


Fig. 11. System equivalent flux densities (SEFD) for the four main RCU modes used by KAIRA.

background. We assume a Galactic emission $T_{\text{sky}} = T_{s0}\lambda^{2.55}$, where $T_{s0} = 60 \pm 20$ K, for Galactic latitudes $10^\circ < b < 90^\circ$ based on established galactic emission models [27]–[29]. For increasing Z , there is a degradation in sensitivity caused by reduced gain of individual dipoles, reduced A_{eff} due to projected coupling, reduced projected collecting area of the phased array, longer path length through the ionosphere, and larger separation of the ionospheric pierce points of the calibrator sources.

Values for SEFD are shown in Fig. 11. Gaps in frequency are where high levels of RFI prevent meaningful measurement. RFI also contributes to larger errors (particularly > 230 MHz), as does uncertainty in the contribution from the Galactic background when the beam size is larger (particularly < 50 MHz).

Changing beam size, array effective area, the difference in sensitivity due to the number of elements ($\text{HBA} = 16 \times \text{LBA}$) and variations in amplifier and filter responses as a function of frequency contribute to the variation in the SEFD. However,

the values we measure are comparable to the values calculated based on component responses [21] and those measured within the International LOFAR telescope [3] for stations of similar size to KAIRA.

IV. SPECIAL OPERATIONAL MODES

Several additional operational modes have been developed specifically at KAIRA to fully develop the capabilities of the station. A number of these are also of interest to the LOFAR community and may, ultimately, be ported to the LOFAR operational system.

A. Mode “357”

Although the complete LBA and HBA arrays cannot be used simultaneously, it is possible to use combinations of subsets to permit observations across the entire frequency capability of the system, albeit with a tradeoff in sensitivity and resolution. In September 2012, KAIRA became the first LOFAR-based facility to operate these three modes simultaneously, i.e., the so-called “mode 357.” RCU mode 6 requires the 160 MHz sampler-clock frequency and so cannot be used simultaneously with the others.

To achieve this, a third of the LBA dipoles were used in combination with a third of the HBA tiles receiving in RCU mode 5 and a further third of the HBA tiles receiving in RCU mode 7. Initially, the dipoles and tiles chosen for each mode corresponded with those connected to a sequential series of RCUs (i.e., LBA dipoles connected to units 0–31, HBA tiles in mode 5 connected to units 32–63 and tiles in mode 7 connected to units 64–95). This results in the use of an inner core of dipoles within the LBA field and two full-length strips of HBA tiles along the long axis of the array, each two tiles wide. Available beamlets were spread such that modes 3 and 5 were each covered by 100 subbands and mode 7 by the remaining 44 to a maximum observing frequency of 244 MHz. Given the limit to the number of available subbands, frequency coverage is not contiguous.

The current implementation of this operational mode uses an outer ring of LBA dipoles and a set of 4×4 tile squares and a further set with a dimension of 4×5 tiles including the empty snow corridor. This results in more even beam shapes than the original configuration.

B. Four-Bit Observing

Eight-bit sampling, allowing the formation of up to 488 beamlets, is now a regular observing mode with LOFAR. However, KAIRA remains the only station using LOFAR hardware to have investigated 4-bit sampling to allow the formation of up to 976 beamlets. The principal advantage of 4-bit sampling is that it allows complete coverage of available frequencies within the filter limits from 10 to 244 MHz for a single pointing direction. The disadvantage is the reduced headroom for observing strong radio sources and identifying RFI. This is a particular issue with LBA observations where the sharp peak

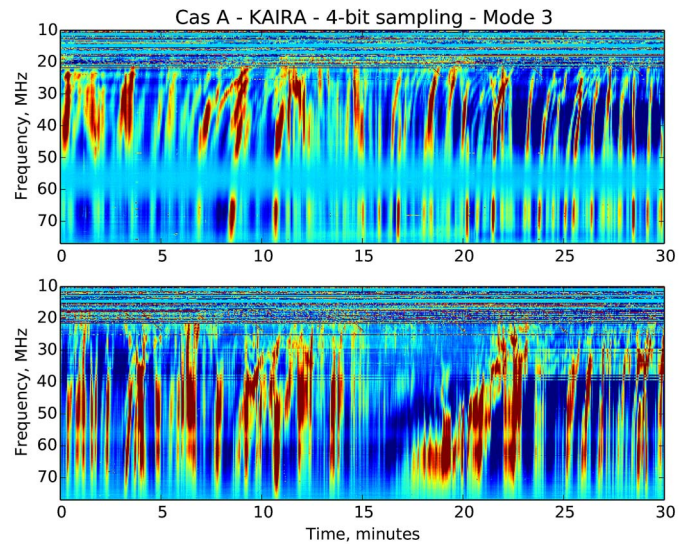


Fig. 12. Mode 357 observation taken using 4-bit sampling of Casiopeia A. The top plot is data with no attenuation applied, the lower plot is data with full attenuation applied. Each plot has been normalized by dividing each frequency channel by its median.

in the antenna response at 58 MHz saturates when observing with 4-bit sampling.

Attenuators can be set to attenuate the signal received by any RCU up to a maximum of 7.75 dB in 0.26 dB steps. This alleviates, but does not completely eliminate, the issue, as can be seen in Fig. 12.

With maximum attenuation of the signals from the LBA dipoles, it can be seen that some signal is recovered over the frequencies of peak response. However, some level of saturation remains as can be seen by the faint “band” centered around 58 MHz in Fig. 12.

Some aliasing of the signal from channels highly contaminated by strong RFI is also apparent under some circumstances. For example, the fainter “banding” apparent in the data between 30 and 40 MHz in, particularly, the lower plot of Fig. 12 may be the result of aliasing of heavily contaminated channels below 20 MHz. The chirp from a transmitter in Cyprus, seen as the periodic diagonal line in dynamic spectra around 20–25 MHz is clearly aliased to ≈ 70 MHz in observations of weaker sources (not shown). It is possible to mitigate this issue by observing using the LBA mode 4 instead of mode 3. This applies a 30–70 MHz filter to exclude the heavy RFI contamination of the lower frequencies.

Fig. 13 shows dynamic spectra of an observation of Casiopeia A taken in mode 4 with 4-bit sampling. The upper plot, with no attenuation applied, shows some apparent aliasing in frequency bands 40–45 MHz. No aliasing is obvious when full attenuation is applied as in the lower plot.

C. Reduced HBA Array Sampling

For incoherent scatter radar measurements, such as those described in Section V-A, the presence of pronounced grating sidelobes from the HBA array is not significant. This is because the transmitted signal from the radar is of known location through the timing, thus removing any directional ambiguity.

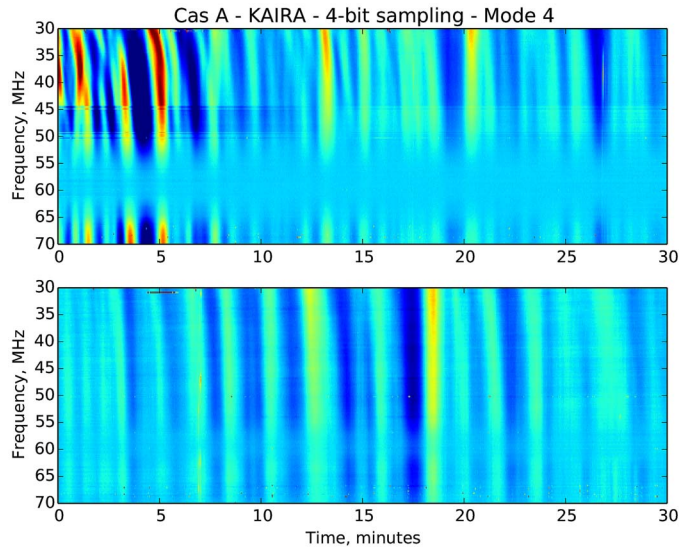


Fig. 13. Mode 357 observation taken using 4-bit sampling of Casiopeia A in LBA mode 4. The top plot is data with no attenuation applied, the lower plot is data with full attenuation applied. Each plot has been normalized by dividing each frequency channel by its median.

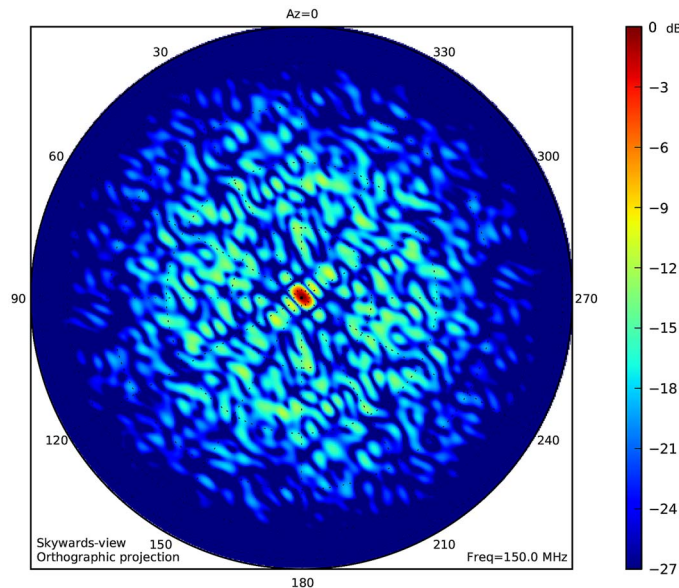


Fig. 14. Simulation of the zenith beam response of the KAIRA HBA array using only one crossed-bowtie antenna element per tile. Compare with Fig. 10.

However for imaging applications, the reduction of grating lobes from the system is necessary. This can be facilitated by using an individual crossed-bowtie antenna element (or subset of antenna elements) from each HBA tile. Using different antenna elements from each tile results in a reduction in the number of redundant baselines, thus improving the instantaneous sidelobe pattern. Additionally, the beams of the individual tiles increase, thus allowing imaging of a larger sky area, albeit at the reduction in sensitivity. Fig. 14 shows a simulated beam pattern of the KAIRA HBA array. The antenna elements selected result in 870 nonredundant baselines (out of a total of 1128).

Additionally, it is possible to increase the vertical size of the beam for incoherent scatter radar experiments. This involves only using a subset of each HBA tile in order to achieve a

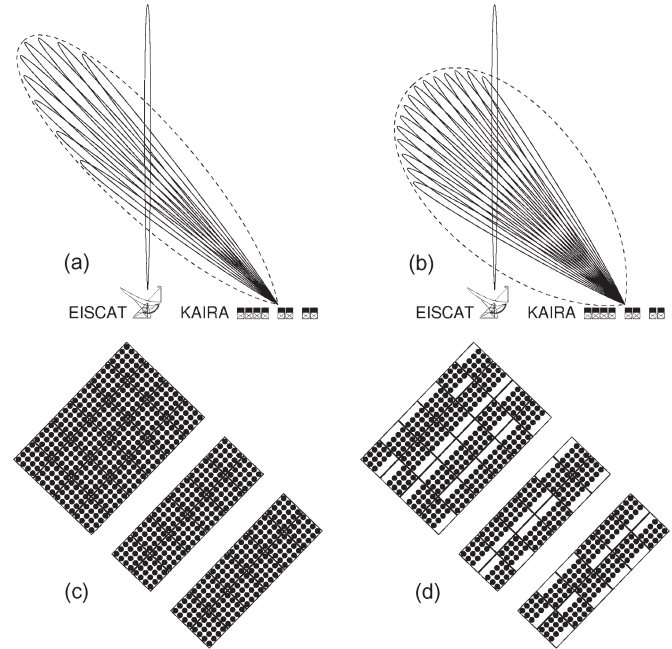


Fig. 15. By using subsets of crossed-bowtie antenna elements within each tile, it is possible to increase the coverage of the Tromsø radar beam. In (a), the full tile set is used, whereas in (b), one quarter of the antenna elements from each tile are not used to broaden the vertical beam. Parts (c) and (d) show the antenna elements used for the two cases, respectively.

broader beam pattern in the vertical direction although with reduced sensitivity. An example of this is shown in Fig. 15. Although not critical for receiving from an artificial signal, different sets can be used within each tile in order to lessen the grating lobe effect.

V. FIRST SCIENTIFIC RESULTS

First observations were carried out in mid-August 2012. During the commissioning phase of the project, and subsequent routine operations, several significant results have been achieved demonstrating not just the capability and function of the instrument, but its scientific potential. The following are a small selection of some of the initial results by way of example.

A. Bistatic Incoherent Scatter Radar

Multistatic incoherent scatter radar measurement capability offers the possibility of instantaneously measuring a full profile of vector velocities, which can be used, e.g., to derive ionospheric neutral winds and electric fields [30]–[32].

To demonstrate that KAIRA can contribute to multistatic incoherent scatter radar measurements, we performed a bistatic radar experiment on August 21, 2012 together with the EISCAT VHF radar in Ramfjordmoen, approximately 85 km northwest from KAIRA. In this experiment, we transmitted an optimized code group [33] of 20 codes with 128 μ s Bd lengths and 10 bits per code. Fig. 16 shows the lag-profile inversion [34] result of a 512-s integration period.

During the experiment, we had 30 dual-polarized beams intersecting the Tromsø VHF vertical beam at altitudes between 90 km and 2000 km. In this plot, we have combined all

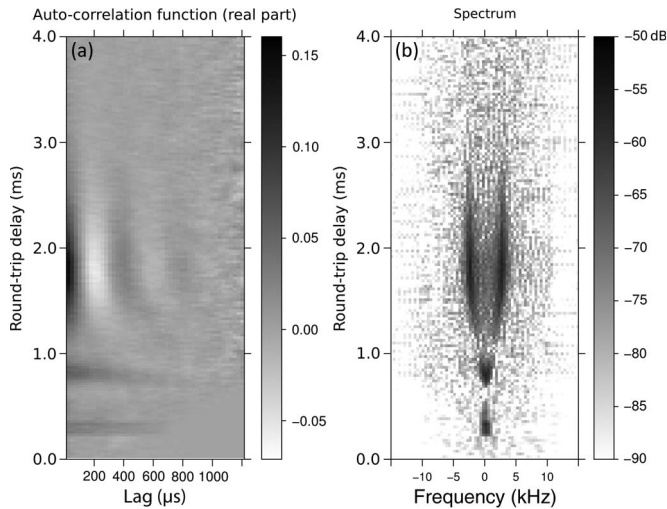


Fig. 16. First multibeam bistatic incoherent scatter radar measurement demonstrating the measurement of the incoherent scatter auto-correlation function (a), and the derived full ionospheric incoherent scatter spectrum profile (b) with respect to the transmitter frequency (224 MHz). The vertical axis is the total round-trip delay of the signal from transmission to reception.

polarizations and beams simply by averaging the autocorrelation functions together and yet still reach altitudes of 400 km. This is not the optimal way of combining the polarizations and beams, and improving this is a topic of future work.

This result constitutes the first true multibeam bistatic incoherent scatter radar measurement against the EISCAT system. This is an important step in its own right, opening up possibilities for multiheight bistatic measurements of the ionosphere. However, it is also important as a technological demonstrator for the proposed EISCAT_3-D system by showing robust measurement results. At this stage, there are no other multibeam receiver systems receiving multiheight incoherent scatter signals, making the KAIRA facility a significant advance in this field.

B. Riometry

A riometer (Relative Ionospheric Opacity Meter for Extra-Terrestrial Emissions of Radio noise) measures the power of radio emissions from the sky at given frequencies. The radio waves are attenuated in the collisional plasma of the ionospheric D region (50–100 km) during ionization events (such as particle precipitation or solar-flare induced photoionization) [35].

The diurnal curve of received noise power is removed from equivalent curves measured during “quiet” (undisturbed) days of the month, resulting in the amount of radio noise absorption, $A = 10 \log_{10}(P_0/P)$, where P_0 is the quiet-day power, P is the observed power, and A is absorption in decibels [36]. The amount of absorption increases with increasing electron density, i.e., n_e , and electron-neutral collision frequency, ν_{en} , which, in turn, is a function of neutral air temperature T , and neutral particle density N : $\nu_{en} \propto N \times T^{1/2}$ [36]. Furthermore, the amount of observed absorption depends upon the observation frequency.

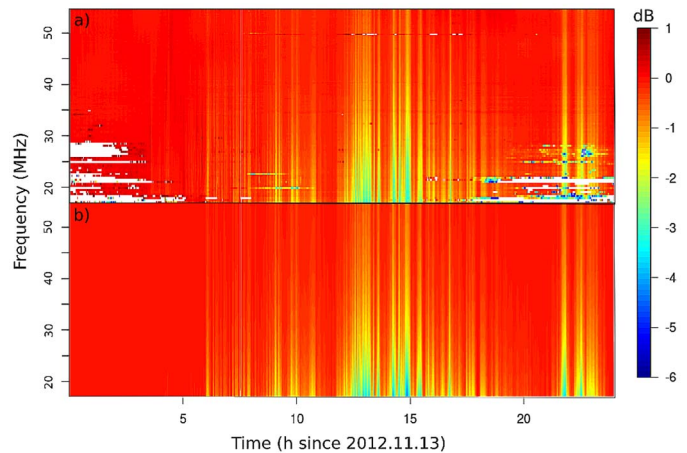


Fig. 17. Measured absorption on the vertical beam of the LBA, starting from 12 UTC on 13 November 2012. The measured absorption is shown above (a), and the forward model, corresponding to the maximum likelihood estimate of an electron density profile is shown below (b).

KAIRA is ideally suited to riometry observations because of its location, multibeam capability, all-sky imaging and multifrequency signal processing over a wide part of the VHF spectrum. Due to the high-latitude location of KAIRA, it will measure frequently occurring D-region electron density enhancements due to high-energy particle precipitation inside the auroral oval and inside the outer radiation belt.

The multibeam capability of KAIRA allows spatially-resolved riometer measurements by using beams with narrow fields-of-view, much in the same way that other imaging riometers [37] function. However, the wide-band nature of KAIRA will allow measurements to be done simultaneously in the frequency range of 10–80 MHz, allowing us to measure the frequency dependence of the absorption, in addition to adding significantly more statistics. To the best of our knowledge, KAIRA is the first wide-band imaging riometer built.

It has been shown by multiple authors [38], [39] that a measurement of frequency dependent riometer absorption can be used to estimate the electron density height profile. This has so far only been done using riometers operating at a few discrete frequencies. KAIRA will be able to perform frequency continuum measurements between 10 and 80 MHz.

In November 2012, KAIRA was observing in wide-band riometer mode during an auroral precipitation event that caused clear absorption of cosmic radio waves. A total of 244 beamlets had been configured to observe a spread of frequencies in the vertical direction. Correcting for the quiet day background, the absorption was measured and is shown in Fig. 17(a). In this case, the quiet day is a measurement performed during a geophysically quiet day (dominated by normal solar photoionization) three days prior to the absorption event.

Because of ever-present RFI, parts of the measurement, particularly below 30 MHz, are corrupted with signals of non-cosmic nature. To remove these, we make the assumption that the variability of the sky-signal with frequency at each instant of time is smooth. We can then use an iterative least-squares fitting procedure to then remove this interference. During each step of the iteration, we fit a third-order polynomial to the power spectrum. Then, outliers are identified. If there is a frequency

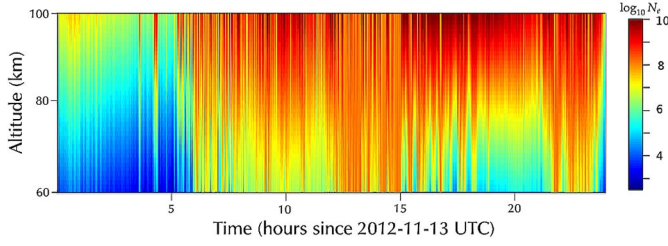


Fig. 18. Fitted electron density ($\log_{10}(N_e/\text{m}^3)$) profile from the data in Fig. 17(a). We used a quadratic polynomial to fit the electron density profile.

bin with power that deviates more than $2.5\text{-}\sigma$ from the least squares polynomial fit, it is tagged as an outlier and removed. Once the iteration is finished, the outliers are discarded from the measurement. In the absence of a way to estimate measurement errors, we estimate a sample variance from the outlier-removed polynomial linear least-squares fit residuals. We used visual inspection of the results to determine that the automatic scheme works to a reasonable degree of accuracy. Also, the best fit for absorption, shown in Fig. 17(b), does not show significant contribution due to RFI, indicating that RFI is properly removed from the measurements.

This frequency dependent absorption can be translated into electron density profiles, as shown in Fig. 18. In order to invert the absorption measurements into electron density profiles, we used a linear least-squares fit to a quadratic polynomial model of electron density [see (1)]. This is similar to the method of Partasarathy *et al.* [38], which assumes a polynomial height profile

$$N_e(r) = \sum_{i=0}^N a_i r^i. \quad (1)$$

In this case, we used the quasi-longitudinal approximation of the Appleton-Hartree equation for the refractive index of magnetoionic plasma. This results in the following measurement equation for radio wave absorption through the D-region of the ionosphere:

$$A(\omega) = c \int_0^{\infty} \frac{\nu(r)}{\nu(r)^2 + (\omega \pm \omega_g)^2} N_e(r) dr \quad (2)$$

where $N_e(r)$ is the electron density at altitude r , $\nu(r)$ is the electron neutral collision frequency at altitude r , ω_g is the electron gyrofrequency, ω is the frequency of the radio wave, and c is a constant.

Instead of using just three measurements to fit three parameters, as was done by Parthasarathy *et al.* [38], we used a linear least-squares fit of all measured frequencies to determine the maximum likelihood quadratic polynomial coefficients of the electron density profile. Due to the ill-posed nature of the problem, we could not fit a higher order polynomial. Thus, the polynomial model for electron density profiles does not allow very much variability in range. This is to some extent an inherent limitation of the riometer inversion. We are currently in the process of developing an improved electron density profile estimation algorithms based on nonlinear least-squares,

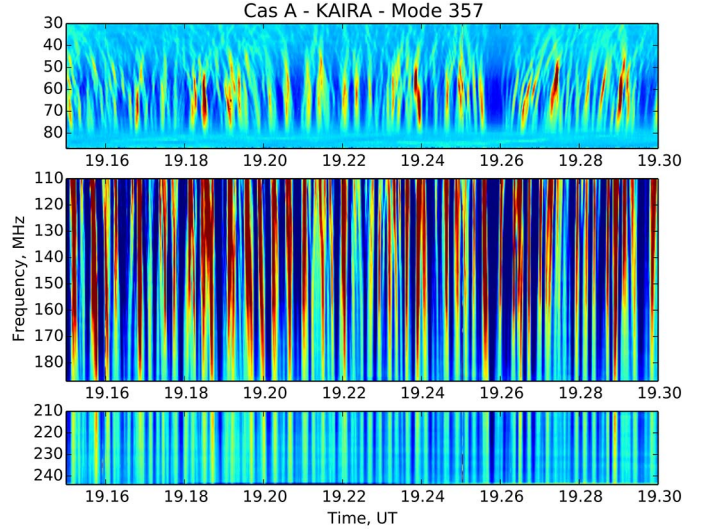


Fig. 19. Dynamic spectrum of data taken during a mode 357 observation of Cygnus-A on 25 September 2012. The data were normalized by dividing each frequency subband by its median.

Bayesian statistics and D-region ionization models [40]. We expect these new models to provide a more realistic representation of the electron density profile.

Thus the KAIRA facility provides a multibeam riometry covering a broad range of frequencies. Although other LOFAR stations are technically capable of conducting riometric measurements using our control and data reduction software, these have not yet been realised. Additionally, only KAIRA is placed at a suitable latitude allowing detailed study of significant ionospheric absorption events. This placement and capability constitute an important step in the advancement of riometric studies.

C. Ionospheric Scintillation

Ionospheric scintillation is the scintillation of the radio signal from a compact source due to scattering and refraction from density variations in the ionosphere. The study of this phenomenon is most often carried out using satellite measurements from GPS and other beacon satellites orbiting the Earth. Such measurements can be used to determine information on the density irregularities giving rise to the scintillation and the effects of these on the radio signal itself [41], information on increasing importance given the modern reliance on satellite communications.

Usually the scattering can be described as “weak” where it can be assumed that the waves diffracted by a “thin” scattering screen do not subsequently interfere between themselves, or “strong”, where this assumption no longer holds true. Larger-scale density variations can also cause the scintillation to be “refractive”, leading to lensing and other effects.

Astronomical radio sources can also exhibit ionospheric scintillation, particularly at lower RFs. Observing such sources offers the advantage over satellite measurements of a very broad range of RFs, allowing dynamic spectra to be created. In Fig. 19 we show a “mode 357” observation of the strong radio source, Cygnus A. The scintillation is readily apparent

and can be seen to be consistent across all the higher KAIRA observing frequencies. If time series are taken for any of the higher frequencies, they would show exactly the same pattern of peaks and troughs simultaneously, indicating a weak scattering regime. Towards the lower frequencies, however, the pattern undergoes obvious changes, indicating the transition to strong scatter. It is evident from these spectra that wide bandwidths are required to observe this transition adequately, something which is only possible with new instruments such as KAIRA.

To the authors' knowledge, this is the first time that this transition has been directly observed in a dynamic spectrum and such measurements are already providing new insights into the study of ionospheric scintillation and the density structures, which give rise to it. The development of this experiment at KAIRA prompted it to be attempted successfully with the full array of LOFAR stations, illustrating the symbiotic relationship between the two projects. This represented the first, and so far only, attempt to use mode 357 with LOFAR.

D. VLBI

Because the KAIRA station is not directly connected to the LOFAR network, it currently cannot participate in standard international LOFAR observations. For certain special projects requiring the highest possible resolution, KAIRA can nevertheless be an important contribution to VLBI with LOFAR and other stations worldwide. The baseline to LOFAR station FR606 (Nançay, France) of 2600 km is twice as long as the longest within LOFAR between stations FR606 and SE607 (Onsala, Sweden).

In March 2013, KAIRA participated in an intercontinental experiment with two LOFAR stations, i.e., SE607 and DE601 (Effelsberg, Germany), and the LWA at about 8000 km distance. The comparatively low sensitivity of these low-band observations and a number of minor technical problems make the analysis difficult, and fringes have not been found yet.

A technical test was performed on May 13, 2013, in which KAIRA and the DE601 LOFAR station (2185-km baseline) observed the bright pulsar B0809+74 in the high band in short blocks of a few minutes each. The following results are based on only 95 s of data between 15:00:08 and 15:01:43 UTC. 48 MHz of bandwidth centered on 143.26 MHz were recorded at both stations. This is the longest baseline result so far achieved between LOFAR-built systems, significantly exceeding the longest current baseline of the International LOFAR Telescope (only 1302 km).

For the correlation our own implementation of a standard FX correlator [42] was used, with geometric delays corrected to an accuracy better than the clock variations of ≈ 20 ns. Visibilities were averaged over 0.1 s and Fourier-transformed for the fringe-detection. For a deeper analysis the visibilities were converted to a circular polarization basis, in which differential Faraday rotation (DFR) does not mix polarizations. A model including DFR, dispersive ionospheric delay, nondispersive delay (clock and geometric offset) and a phase rate was fitted to data blocks of 9.4 s using a newly developed gridding algorithm (to be published). The nonstandard dipole orientations (see Section III-C) was not understood then, but noticed in the

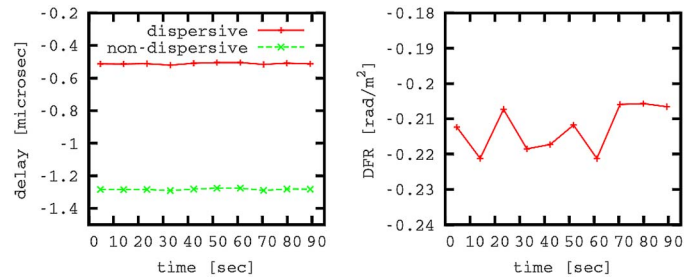


Fig. 20. Parameters of Effelsberg-KAIRA fringes as a function of time. Left: Dispersive and nondispersive delay, the former for a reference frequency of 143 MHz. Right: Differential Faraday rotation (DFR).

process. The orientation was included as an additional free parameter and recovered to within 7° , even though the effect is highly degenerate with DFR. This parameter was then fixed and the remaining ones fitted as a function of time. Fig. 20 shows some of the results.

The nondispersive delay of $-1.3 \mu\text{s}$ is mostly due to a known offset in Effelsberg. The other parameters can be compared with predictions from ionospheric models using similar methods as described by [43]. The prediction for DFR agrees almost exactly with the measured value of -0.21 rad/m^2 . For the dispersive delay, the prediction of $-0.59 \mu\text{s}$ is still very close to the measured value of $-0.51 \mu\text{s}$.

This does not only confirm that we understand the instrumental properties well, but also that (at least in this experiment) the ionosphere is sufficiently benign to permit a robust and stable calibration and to do low-frequency VLBI on baselines of several thousand kilometers.

VI. CONCLUSION

The KAIRA facility has been successfully built and is operational. Both antenna arrays have been commissioned and the station has been used for VHF incoherent scatter radar reception, thus demonstrating its suitability for EISCAT_3-D. Additionally, wide-band multibeam riometry and ionospheric scintillation experiments are being routinely carried out, and we have demonstrated very long baseline interferometric fringes, indicating not just technical performance and calibration, but also compatibility with other radio telescope systems. We show that the use of this form of radio astronomical technology has a direct and effective application to geoscience experiments, such as riometry and scintillation studies. Due to the flexibility of the underlying technology, many other possible types of new innovative experiments are anticipated.

ACKNOWLEDGMENT

The authors would like to thank the staff of both Sodankylä Geophysical Observatory, Finland, and the Netherlands Institute for Radio Astronomy (ASTRON). The authors also thank H. Wessels, S. Keenan, and A. Jutila and the teams of summer students who assisted with the build. The authors also thank the support provided by Rutherford Appleton Laboratory, UK, and also Kilpisjärvi Biological Station of the University of Helsinki, Finland. EISCAT is an international association supported by

China (CRIRP), Finland (SA), Germany (DFG), Japan (STEL and NIPR), Norway (NFR), Sweden (VR), and the United Kingdom (NERC).

REFERENCES

- [1] H. Rishbeth and P. Williams, "The EISCAT ionospheric radar: The system and its early results," *Q. J. R. Astron. Soc.*, vol. 26, pp. 478–512, Dec. 1985.
- [2] T. Ulich, A. Aikio, I. McCrea, and E. Turunen, "EISCAT_3D: The European three-dimensional imaging radar for atmospheric and geospace research," in *Proc. 38th COSPAR Sci. Assem.*, vol. 38, *COSPAR Meeting*, 2010, p. 873.
- [3] M. P. van Haarlem *et al.*, "LOFAR: The low-frequency array," *Astron. Astrophys.*, vol. 556, p. A2, 2013.
- [4] C.-F. Enell *et al.*, "Effects of D-region RF heating studied with the Sodankylä Ion Chemistry model," *Annales Geophys.*, vol. 23, no. 5, pp. 1575–1583, 2005.
- [5] A. Kero, T. Bösinger, P. Pollari, E. Turunen, and M. Rietveld, "First EISCAT measurement of electron-gas temperature in the artificially heated D-region ionosphere," *Annales Geophys.*, vol. 18, no. 9, pp. 1210–1215, 2000.
- [6] A. Senior, M. T. Rietveld, F. Honary, W. Singer, and M. J. Kosch, "Measurements and modeling of cosmic noise absorption changes due to radio heating of the D region ionosphere," *J. Geophys. Res., Space Phys.*, vol. 116, p. A04310, 2011.
- [7] S. Close, M. Oppenheim, S. Hunt, and L. Dyrud, "Scattering characteristics of high-resolution meteor head echoes detected at multiple frequencies," *J. Geophys. Res., Space Phys.*, vol. 107, no. A10, pp. SIA 9-1–SIA 9-12, Oct. 2002.
- [8] A. Hewish, P. F. Scott, and D. Wills, "Interplanetary scintillation of small diameter radio sources," *Nature*, vol. 203, pp. 1214–1217, Sep. 1964.
- [9] R. A. Fallows, A. Asgekar, M. M. Bisi, A. R. Breen, and S. ter-Veen, "The dynamic spectrum of interplanetary scintillation: First solar wind observations on lofar," *Solar Phys.*, vol. 285, no. 1/2, pp. 127–139, 2013.
- [10] J.-P. Raulin and A. A. Pacini, "Solar radio emissions," *Adv. Space Res.*, vol. 35, pp. 739–754, 2005.
- [11] N. Meyer-Vernet, G. Daigne, and A. Lecacheux, "Dynamic spectra of some terrestrial ionospheric effects at decametric wavelengths—Applications in other astrophysical contexts," *Astron. Astrophys.*, vol. 96, pp. 296–301, Mar. 1981.
- [12] M. C. Kelley, D. T. Farley, and J. Röttger, "The effect of cluster ions on anomalous VHF backscatter from the summer polar mesosphere," *Geophys. Res. Lett.*, vol. 14, no. 10, pp. 1031–1034, 1987.
- [13] O. Wucknitz, "e-VLBI with LOFAR," in *Proc. 10th Eur. VLBI Netw. Symp. EVN Users Meet., VLBI New Gener. Radio Arrays*, 2010. [Online]. Available: <http://pos.sissa.it/cgi-bin/reader/conf.cgi?confid=125>
- [14] P. E. Dewdney, P. J. Hall, R. T. Schilizzi, and T. J. L. W. Lazio, "The square kilometre array," *IEEE Proc.*, vol. 97, pp. 1482–1496, Aug. 2009.
- [15] R. T. Schilizzi, P. E. F. Dewdney, and T. J. W. Lazio, "The square kilometre array," in *Proc. SPIE Conf. Series*, Jul. 2010, vol. 7733.
- [16] S. J. Tingay *et al.*, "The Murchison Widefield array: The square kilometre array precursor at low radio frequencies," *Publ. ASA*, vol. 30, pp. 1–22, Jan. 2013.
- [17] C. J. Lonsdale *et al.*, "The murchison widefield array: Design overview," *Proc. IEEE*, vol. 97, no. 8, pp. 1497–1506, Aug. 2009.
- [18] S. W. Ellingson *et al.*, "The long wavelength array," *Proc. IEEE*, vol. 97, no. 8, pp. 1421–1430, Aug. 2009.
- [19] M. de Vos, A. W. Gunst, and R. Nijboer, "The LOFAR telescope: System architecture and signal processing," *Proc. IEEE*, vol. 97, no. 8, pp. 1431–1437, Aug. 2009.
- [20] I. I. Virtanen, *Station Data Cookbook*, May 2012.
- [21] M. J. Norden and G. W. Kant, "RCU II signal analysis and specification," Astron, Dwingeloo, The Netherlands, May 2007.
- [22] M. Orispää and S. Lehtinen, "FORTRAN Linear Inverse Problem Solver," *Inverse Problems Imag.*, vol. 4, no. 3, pp. 485–503, 2010.
- [23] G. B. Taylor, C. L. Carilli, and R. A. Perley, Eds., *Synthesis Imaging in Radio Astronomy II*, vol. 180. Astronomical Society of the Pacific, 1999, ser. Astronomical Society of the Pacific Conference Series.
- [24] R. J. Nijboer and J. E. Noordam, "LOFAR Calibration," in *Astronomical Data Analysis Software and Systems XVI*, vol. 376, ser. Astronomical Society of the Pacific Conference Series, R. A. Shaw, F. Hill, and D. J. Bell, Eds., Oct. 2007, p. 237.
- [25] J. W. M. Baars, R. Genzel, I. I. K. Pauliny-Toth, and A. Witzel, "The absolute spectrum of CAS A—An accurate flux density scale and a set of secondary calibrators," *Astron. Astrophys.*, vol. 61, pp. 99–106, Oct. 1977.
- [26] J. F. Helmboldt and N. E. Kassim, "The evolution of Cassiopeia A at low radio frequencies," *Astron. J.*, vol. 138, pp. 838–844, Sep. 2009.
- [27] R. S. Roger, C. H. Costain, T. L. Landecker, and C. M. Swerdlyk, "The radio emission from the galaxy at 22 mhz," *Astron. Astrophys.*, vol. 137, pp. 7–19, May 1999.
- [28] A. de Oliveira-Costa *et al.*, "A model of diffuse Galactic radio emission from 10 MHz to 100 GHz," *MNRAS*, vol. 388, pp. 247–260, Jul. 2008.
- [29] A. E. Guzmán, J. May, H. Alvarez, and K. Maeda, "All-sky Galactic radiation at 45 MHz and spectral index between 45 and 408 MHz," *Astron. Astrophys.*, vol. 525, p. A138, Jan. 2011.
- [30] T. Nygrén, A. T. Aikio, R. Kuula, and M. Voiculescu, "Electric fields and neutral winds from monostatic incoherent scatter measurements by means of stochastic inversion," *J. Geophys. Res. (Space Physics)*, vol. 116, no. A5, p. 5305, May 2011.
- [31] C. J. Heinselman and M. J. Nicolls, "A Bayesian approach to electric field and E-region neutral wind estimation with the Poker Flat Advanced Modular Incoherent Scatter Radar," *Radio Sci.*, vol. 43, no. 5, p. 5013, Oct. 2008.
- [32] M. J. Nicolls *et al.*, "High-resolution electron temperature measurements using the plasma line asymmetry," *Geophys. Res. Lett.*, vol. 33, no. 18, pp. L18107-1–L18107-5, 2006.
- [33] J. Vierinen, M. S. Lehtinen, M. Orispää, and I. I. Virtanen, "Transmission code optimization method for incoherent scatter radar," *Annales Geophys.*, vol. 26, no. 9, pp. 2923–2927, 2008.
- [34] I. I. Virtanen, M. S. Lehtinen, T. Nygrén, M. Orispää, and J. Vierinen, "Lag profile inversion method for EISCAT data analysis," *Annales Geophys.*, vol. 26, pp. 571–581, Mar. 2008.
- [35] C. G. Little and H. Leinbach, "The riometer—A device for continuous measurement of ionospheric absorption," *Proc. IRE*, vol. 47, pp. 315–320, 1959.
- [36] T. J. Rosenberg, D. L. Detrick, H. Ranta, and A. Ranta, "Autumn and winter anomalies in ionospheric absorption as measured by riometers," *J. Atmos. Terrestrial Phys.*, vol. 45, pp. 193–202, Apr. 1983.
- [37] F. Honary *et al.*, "Invited Article: Digital beam-forming imaging riometer systems," *Rev. Sci. Instrum.*, vol. 82, no. 3, p. 031301, Mar. 2011.
- [38] R. Parthasarathy, G. M. Lerfald, and C. G. Little, "Derivation of electron-density profiles in the lower ionosphere using radio absorption measurements at multiple frequencies," *Geophys. Res. Lett.*, vol. 68, no. 12, pp. 3581–3588, Jun. 1963.
- [39] V. V. Belikovitch, M. A. Itkina, and L. V. Rodygin, "Determination of the electron concentration profile in the lower ionosphere from the absorption frequency variation," *Geomagn. Aeronomy*, vol. 4, no. 612, p. 610, 1964.
- [40] A. Kero *et al.*, "Ionospheric electron density profiles inverted from a spectral riometer measurement," *J. Geophys. Res.*, vol. 41, no. 15, pp. 5370–5375, Aug. 2014.
- [41] B. Forte, "Refractive scattering evidence from multifrequency scintillation spectra observed at auroral latitudes," *Radio Sci.*, vol. 43, no. 2, p. 2012, Apr. 2008.
- [42] J. D. Romney, "Cross Correlators," in *Proc. Synthesis Imag. Radio Astron. II*, vol. 180, ser. Astronomical Society of the Pacific Conference Series, G. B. Taylor, C. L. Carilli, and R. A. Perley, Eds., 1999, p. 57.
- [43] C. Sotomayor-Beltran *et al.*, "Calibrating high-precision Faraday rotation measurements for LOFAR and the next generation of low-frequency radio telescopes," *Astron. Astrophys.*, vol. 552, pp. A58-1–A58-13, Apr. 2013.

Authors' photographs and biographies not available at the time of publication.